Cooperative self-assembly process involving giant toroidal polyoxometalate as a membrane building block in nanoscale vesicles

Clément Falaise, Soumaya Khlifi, Pierre Bauduin, Philipp Schmid, Jéril Degrouard, Amélie Leforestier, William Shepard, Jérôme Marrot, Mohamed Haouas, David Landy, et al.

Cooperative Self-Assembly Process involving Giant Toroidal Polyoxometalate as Membrane Building Block in Nanoscale Vesicles

Clément Falaise,[§] Soumaya Khlifi,[§] Pierre Bauduin,[¥] Philipp Schmid,[¥] Jéril Degrouard,[ʃ] Amélie Leforestier,[ʃ] William Shepard,[‡] Jérôme Marrot,[§] Mohamed Haouas,[§] David Landy,[£] Caroline Mellot-Draznieks[†] and Emmanuel Cadot[§*]

§ Institut Lavoisier de Versailles, CNRS, UVSQ, Université Paris-Saclay, Versailles, France
¥ ICSM, CEA, CNRS, ENSCM, Université Montpellier, 34199 Marcoule, France
ʃ Laboratoire de Physique des Solides (LPS), UMR 8502 CNRS, Université Paris-Saclay, Orsay, France
‡ Synchrotron SOLEIL, L'Orme des Merisiers, Saint-Aubain BP 48, 91192 Gif-sur-Yvette, CEDEX, France
£ Unité de Chimie Environnementale et Interactions sur le Vivant (UCEIV, EA 4492), ULCO, Dunkerque, France
† Laboratoire de Chimie des Processus Biologiques, UMR CNRS 8229, Collège de France, Sorbonne Université, PSL Research University, 75231 Paris, Cedex 05, France

ABSTRACT: The self-assembly of organic amphiphilic species into various aggregates such as spherical or elongated micelles, cylinders up to the formation of lyotropic hexagonal or lamellar phases results from cooperative processes orchestrated by hydrophobic effect, while those involving ionic inorganic polynuclear entities and non-ionic organic components are still intriguing. Herein, we report on the supramolecular behavior of giant toroidal molybdenum blue-type polyoxometalate (POM), namely the {Mo_{154}} species in the presence of n-octyl-β–glucoside (C8G1), widely used as surfactant in biochemistry. Structural investigations were carried out using a set of complementary multiscale methods including single-crystal X-ray diffraction analysis supported by molecular modelling, small-angle X-ray scattering (SAXS), and cryo-TEM observations. In addition, liquid NMR, viscosimetry, surface tension measurement, and isothermal titration calorimetry (ITC) provided further information to decipher the complex aggregation pathway. Elucidation of the assembly process reveals a rich scenario where the presence of the large {Mo_{154}} anion disrupts the self-assembly of the C8G1, well-known to produce micelles, and induces striking successive phase transitions from fluid-to-gel and from gel-to-fluid. Herein, intimate organic-inorganic primary interactions arising from the super-chaotropic nature of the {Mo_{154}} lead to versatile nanoscopic hybrid C8G1-{Mo_{154}} aggregates including crystalline discrete assemblies, smectic lamellar liquid crystals, and large uni- or multilamellar vesicles where the large torus {Mo_{154}} type POM acts a trans-membrane component.

INTRODUCTION

The ability of biochemical substances such as phospholipids, glycans, or proteins to interact with discrete inorganic species is essential for some biological functions or applications.[1–3] Knowledge of their primary interactions is also essential to fully understand the biological mechanisms underlying the effectiveness of metallodrugs.[4,5] In context, concepts of supramolecular chemistry offer the possibility of designing synthetic systems able to mimic or model specific short-range intermolecular interactions which contribute to the formation of complex self-assemblies.[6,7,8] Then, designing supramolecular hybrid architectures including dynamics and responsive behavior requires a fine balance between the conglomerate of weak intermolecular forces such as electrostatic, ion-dipole, dipole-dipole, hydrogen-bonding, dispersion, etc., that drives the aggregation processes owing to specific supramolecular recognition.[9] Recent reports highlight the intriguing properties of certain inorganic polynuclear anions, such as polyoxometalates (POMs) or polynuclear clusters for their extremely high propensity to interact strongly in aqueous solution with zwitterionic lipids[10] or non-ionic organic components such as glucoside-based or polyethylene glycol (PEG)-based surfactants or macrocycles (cyclodextrins or cucurbiturils).[11–15] Thermochemical studies supported by theoretical calculations indicated that the chaotropic nature of these ionic species was responsible for these aggregation phenomena, leading to the extension of the Hofmeister series beyond the classical anions

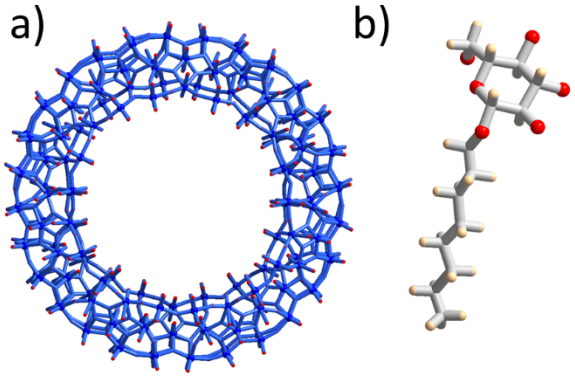

Figure 1. Structural representation of a) the Mo-blue ring-shaped anion $[Mo_{154}O_{462}H_{14}(H_2O)_{70}]^{14-}$ (abbreviated {Mo_{154}}) and b) the n-octyl-β–glucoside, $C_{14}H_{26}O_6$, noted C8G1, showing the hydrophilic glucosidic head, noted G1 and the hydrophobic octyl chain (noted C8). The {Mo_{154}} has an outer diameter of about 36 Å while the unfolded amphiphilic C8G1 is about 14-15 Å in length.

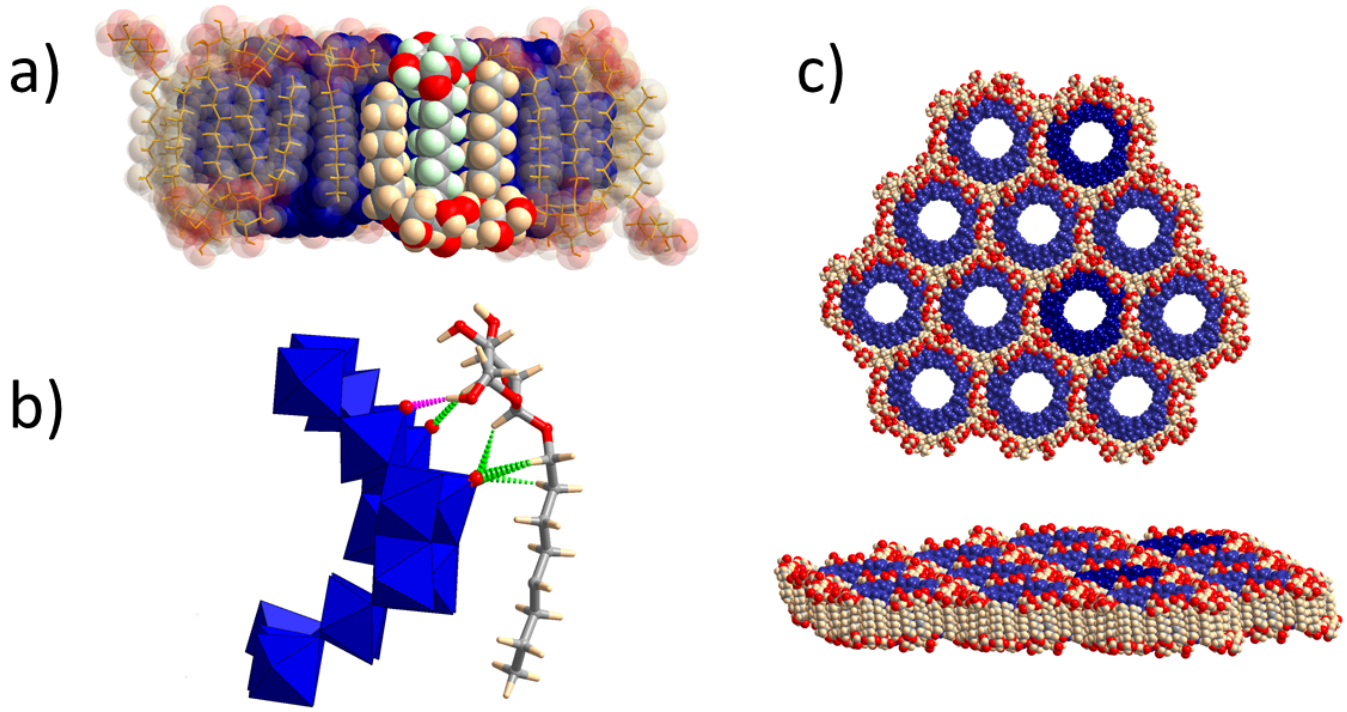

Figure 2. Structural representations of the C8G1-{Mo_{154}} system resulting from the X-ray diffraction analysis and molecular modelling. a) Mixed representation showing the {Mo_{154}} ring-shaped anion (blue spheres) surrounded by 26 C8G1 units (space-filling model and stick representation) which are paralleled grafted on the outer surface of the torus, adopting a strict head-to-tail disposition. b) Each C8G1 unit interacts with the {Mo_{154}} surface through hydrogen bonds involving the G1 hydrophilic head through either hydroxyl groups (dotted pink line) or C-H bonds (dotted light-green line) and some terminal oxo and aquo groups of the inorganic part, while the octyl chains flattened on the {Mo_{154}} outer surface through non-bonding contacts. c) The crystal packing is built from the stacking of 2D hexagonal arrangements wherein the C8G1 surfactants are intercalated between the {Mo_{154}} tori.

(SCN^-, ClO_4^-, etc.).[16–17] Besides, the magnitude of the chaotropic effect correlates well with the variation of the charge density along the archetypical Keggin-type POM series.[18] Recently, the Mo-blue ring-shaped giant anion[19,20] $[Mo_{154}O_{462}H_{14}(H_2O)_{70}]^{14-}$ (abbreviated {Mo_{154}} hereafter) has been identified experimentally as the most super-chaotropic POM species.[21] Moreover, such a ranking within the Hofmeister series is supported by counter-intuitive behaviors whereby the super-chaotropic effect overcomes the expected unfavorable electrostatic repulsions.[22–25]

Here we report on the solution behavior of the super-chaotropic wheel-shaped polyoxometalate {Mo_{154}} in the presence of a non-ionic surfactant, namely n-octyl-β-glucoside abbreviated hereafter C8G1 (see Figure 1). C8G1 is an amphiphilic molecule widely used in biochemistry, especially in the extracting processes of membrane proteins from biological matters.[26,27] C8G1 is an amphiphilic species exhibiting high critical micellar concentration (*cmc* ≈ 25 mM at 25 °C) with a high aggregation number which varies from $N_{Agg} = 80$ to above 130 upon increasing concentration above *cmc*.[26,28] Besides, due to the relative rigidity of the glycoside hydrophilic head, C8G1 has been used frequently as building block either for the preparation of large unilamellar vesicles or for modelling biomembrane systems that integrate membrane proteins.[29,30] Alternatively, C8G1 is used also as an ingredient in the crystallization of membrane proteins.[31] Furthermore, previous studies report on the high affinity of some archetypal POMs such as the super-chaotropic Keggin-type anion $[PW_{12}O_{40}]^{3-}$ with the C8G1 surfactant.[16,32] Herein, the C8G1-{Mo_{154}} supramolecular interactions and related structures were evidenced through a set of complementary methods such as single-crystal X-ray diffraction analysis assisted by molecular modelling, small-angle X-ray scattering, and cryo-TEM observations. Furthermore, surface tension measurement using the Du Noüy ring technique, fluid viscosity measurement, ^{1}H NMR including DOSY, and isothermal titration calorimetry allow us to unravel a multiscale picture of the self-assembly behavior from the discrete species until the structure of large single-walled porous vesicles.

RESULTS AND DISCUSSION

Structural model in the solid-state. Single-crystal X-ray diffraction analysis supported by molecular modelling was used to get definitive structural insights about the primary interactions that drive the self-assembly process between the C8G1 surfactants and the large {Mo_{154}} ring-shaped anion (Figure 2). Single-crystals containing both C8G1 surfactants and the {Mo_{154}} were obtained from synthetic aqueous mixture containing starting materials, that are sodium molybdate, reducing agent (sodium dithionite), and C8G1 at pH 1. The applied synthetic conditions were similar to those previously described by Müller *et al.*, except for the presence of the C8G1 surfactant.[20] These conditions corresponded to 1.4 mM in {Mo_{154}} in the presence of 18 mM C8G1 aqueous solution, which is close to the critical aggregation concentration (about 15 mM) where the {Mo_{154}}-C8G1 hybrid aggregates forms (see the section below). Then, the resulting solution was allowed to stand for crystallization giving very small dark-blue

single crystals $Na_{14}\{Mo_{154}O_{462}H_{14}(H_2O)_{70}\}\cdot 15C8G1.70H_2O$ within 4 days. X-ray diffraction experiments were conducted using synchrotron X-ray source (see Supporting Information, SI, section 1.2.8 and 1.3.3 for further details). It should be noted that the crystallographic *P*-1 space group imposed by the large and symmetric $\{Mo_{154}\}$ ring (D_{7d} point group) of high electron density generates artificially L-C8G1 enantiomers, although only D-C8G1 molecules were used in the synthesis and are therefore present in the crystal. At this stage, the structure refinement revealed remaining electronic density matching in size and shape with unfolded disordered and incomplete alkyl chains, which should thus correspond to the six remaining C8G1 units (over the 15 expected from the elemental analysis). Then, the use of force field-based molecular modelling methods made it possible i) to complete the crystal structure with the localization of the six missing C8G1 units relying on the unrefined electronic density of disordered alkyl chains for their positioning, but also ii) to adjust/optimize the structure by considering the absolute configuration of D-C8G1. The six missing C8G1 units were introduced sequentially as follows. First, each missing C8G1 unit was manually placed with respect to the already identified C8G1 units so as to extend the existing head-to-tail ordering of their hydrophilic heads while overlapping the unrefined electronic density. The resulting structure was then further geometry optimized allowing the relaxation of all atoms including the 15 D-C8G1 units (see SI, section 1.3.4).

The resulting structure analysis reveals an unprecedented hybrid assembly based on the $\{Mo_{154}\}$-shaped wheel decorated by C8G1 surfactants. A total of 26 units were found tightly stacked on its external surface to form a spectacular doughnut-shaped hybrid assembly (see Figure 2a). The C8G1 units are packed around each large torus, arranged in a strict head-to-tail mode in which the glucosidic heads alternate regularly between both opposite faces of the torus. Furthermore, in such an arrangement, the C8G1 units adopt the curvature of the $\{Mo_{154}\}$ outer surface whereby the C8 octyl chains are aligned and appear lying along the outer surface through non-bonding contacts (C-H···O > 3.6 Å). While the van der Waals interactions stabilize such a dense packing, the hydroxyl and C-H groups of the G1 hydrophilic heads were found to interact through weak hydrogen bonds with outward terminal aqua ligands or oxo groups mostly located toward the aperture of the inorganic wheel. These hydrogen-bonding interactions are found within typical interatomic distances range, i.e., O-H···O = ~ 2.75 Å and C-H···O = 3.20-3.40 Å (see Figure 2b). The disposition of the 26 amphiphilic C8G1 units reveals hydrophilic regions of the $\{Mo_{154}\}$ anion where hydrogen bonds are found at the external edge of the torus, while lipophilic domains are located mainly around the torus in the vicinity of the C8 alkyl chains. Remarkably, it is worth noting that such head-to-tail arrangement is reminiscent of those previously observed within crystal structures of pure C8G1.[33–35] The hydroxyl and C-H groups of the G1 hydrophilic heads were found to interact through weak hydrogen bonds with outward terminal aqua ligands or oxo groups mostly located toward the aperture of the inorganic wheel.

In addition, as the 26 C8G1 species fill the space around the anionic wheel, they are shared with the adjacent $\{Mo_{154}\}$ units which pave 2D planes in a quasi-hexagonal fashion (see Figure 2c). The electric balance is ensured by sodium cations which were not located within the structure, due to severe disorders with water molecules, as usually observed in such a type of structures. Interestingly, the packing appears dominated by the supramolecular interactions, dictated here by the super-chaotropic nature of the $\{Mo_{154}\}$ ring-shaped anion and reinforced by the close-packing of the octyl chains arising from a hydrophobic effect. At last, this crystal structure evidences intimate specific interactions between the $\{Mo_{154}\}$ macrocyclic anion and the non-ionic C8G1 amphiphiles. Based on this solid-state observation, we anticipated that $\{Mo_{154}\}$ strongly interacts with C8G1 and therefore disrupts the formation of C8G1 micelles leading to new types of hybrid organic-inorganic aggregates in solution. Therefore, we set out to explore the solution behavior of $\{Mo_{154}\}$/C8G1 mixtures using techniques delivering insights on the short- and long-range spatial organization between the building blocks.

Small Angle X-ray Scattering (SAXS). SAXS technique appears appropriate to characterize such systems since the inorganic nano-wheel $\{Mo_{154}\}$ contains high electron-density Mo element that scatters X-rays strongly and produces specific constructive and destructive interferences related to its ring shape.[21,36,37] In addition, SAXS data not only contain form factor information related to the size and shape of the individual and assembled $\{Mo_{154}\}$ entities but also provide insights into intermolecular interactions between scattering particles given within the structure factor (see SI. section 1.2.7 and 1.3.2 for details about experimental details).

At first, SAXS investigations have been carried out on equilibrated solutions at room temperature containing 1 mM of $\{Mo_{154}\}$ and various concentrations of C8G1 (from 1 to 80 mM) (see Figure 3). Interestingly, the $\{Mo_{154}\}$/C8G1 solutions reveal the existence of narrow gelling domains for C8G1 concentrations ranging from 30-40 mM.

The SAXS scattering curves of the $\{Mo_{154}\}$/C8G1 system revealed three distinct domains. In this first regime ranging between 1 to 20 mM, the SAXS pattern of $\{Mo_{154}\}$ appears almost unaffected by the presence of C8G1. Scattering data are representative of monodisperse isolated $\{Mo_{154}\}$ entities, featured by oscillations located at 2, 4 and 6 nm^{-1} (see Figure 3a) which match fairly well with the simulated scattering curve, e.g. form factor of $\{Mo_{154}\}$.[21] However, drastic alterations of the scattering profiles are observed for C8G1 concentrations between 30 to 40 mM. Indeed, a large increase of the scattered intensity is observed at $q < 2$ nm^{-1} suggesting assembly of the $\{Mo_{154}\}$. At higher q, the $\{Mo_{154}\}$ form factor is unchanged, indicating that the $\{Mo_{154}\}$ keeps it molecular integrity upon addition of C8G1. As supramolecular interactions between $\{Mo_{154}\}$ entities are evidenced by the increase of the scattered intensity at low *q* value, a long-range ordering is identified clearly, giving rise to three non-ambiguous Bragg peaks in the low *q* region (0.25 to 1 nm^{-1}). These Bragg peaks can be indexed as the *001*, *002* and *003* reflections arising from a one-dimensional ordered stack. Moreover, the decrease in scattering intensity of these *00l* peaks supported by the increase in the linewidth with *l* indicates unambiguously the presence of lamellar phases. The gradual shift of the Bragg peaks towards low angles as the C8G1 concentration increases is fairly consistent with the increase of the interlamellar distance from 8 to 12 nm. Besides, the average number of stacked layers has been estimated to be about 5 by using the Scherrer relation and the linewidths of the Bragg peaks. Obviously, the structure of this $\{Mo_{154}\}$/C8G1 mesophase cannot be fully elucidated, but a structural model can be reasonably proposed considering i) the experimental structure resulting from the X-

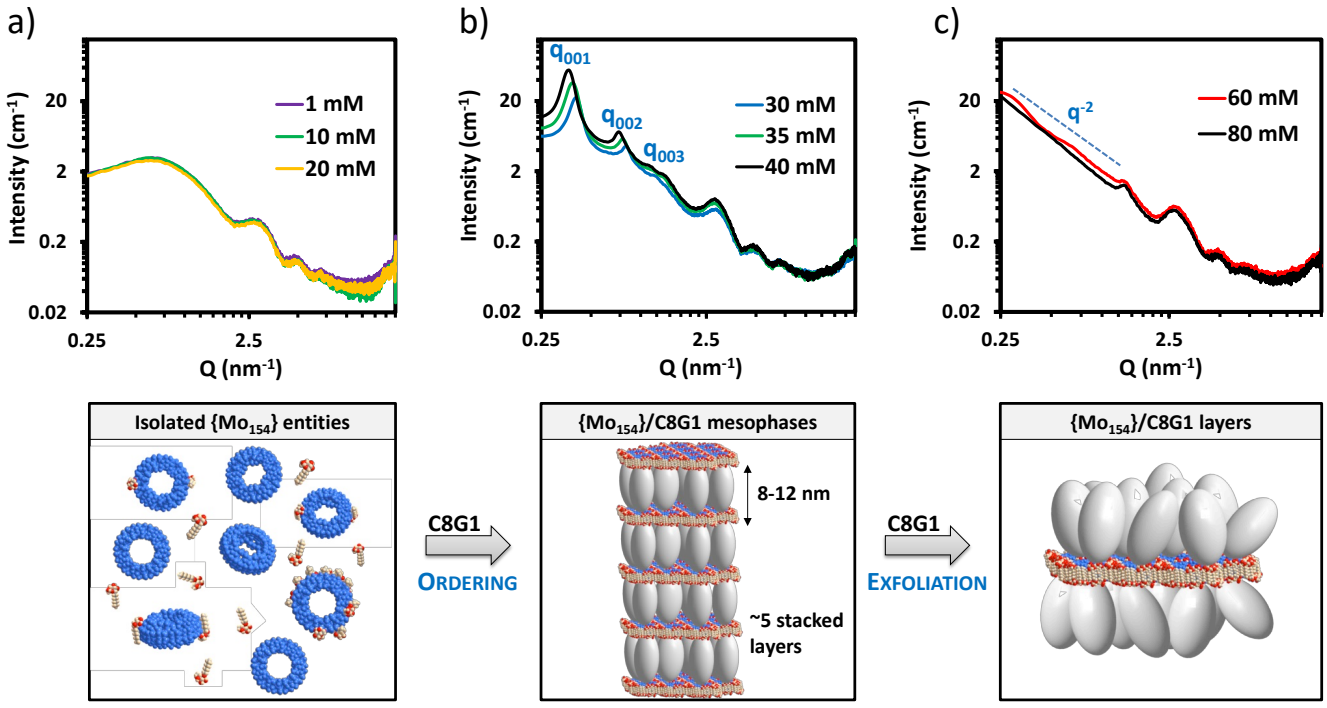

Figure 3. Small angle X-ray scattering curves of {Mo_{154}}/C8G1 mixtures containing 1 mM {Mo_{154}} and variable concentration of C8G1 surfactant, highlighting important change of structure factor with the increasing of C8G1 concentration. a) Up to 20 mM C8G1, {Mo_{154}} entities (blue rings) are isolated from each other. b) Between 30 to 40 mM C8G1, SAXS curves exhibit Bragg peaks featuring the existence of ordered lamellar mesophases that are probably built from hybrid {Mo_{154}}-C8G1 layers and C8G1 micelles (grey ellipsoid). c) The slope at low q region indicates the mixtures containing high C8G1 concentration (> 60 mM) are dominated by {Mo_{154}} based layers that can result from the exfoliation process of hybrid {Mo_{154}}-C8G1 lamellar mesophases.

ray diffraction and modelling analysis which evidenced {Mo_{154}} and C8G1 can self-assemble into 2D hybrid planes (see Figure 2c). Moreover, the {Mo_{154}} ion exhibits high propensity to produce structures resulting from the {Mo_{154}} paving motif into 2D hexagonal planes; ii) the concomitant growth of oblate C8G1-based micelles which exhibit a larger polar radius varying gradually from 4.5 to 6 nm with a concentration of C8G1, while the smaller equatorial radius remains nearly constant around 1.2-1.3 nm.[38] Actually, the formation of micelles above the *cmc* is well documented for the non-ionic C8G1 surfactant. Using complementary techniques such as small angle neutrons scattering (SANS),[38] viscosimetry, tensiometry, calorimetry, vapor pressure, and diffusion analyses, it was shown that aggregation number of C8G1-based micelles can vary from 80 up to 130 units as a result of an increase in micellar size with surfactant concentration.[26] Based on these considerations, we make the hypothesis that the formation of the C8G1/{Mo_{154}} lamellar mesophase results from interactions between {Mo_{154}}-based planes and rod-like micelles that stack into multi (hybrid) layers with interlamellar spaces containing C8G1-based rod-like micelles (see Figure 3b). Besides, the size of the diffraction domain can be determined by using the Scherrer relationship upon the linewidth of the Bragg peaks observed at q_{001} and q_{002}. Thus, such an analysis is rather consistent with a smectic phase which does not exceed about 40-50 nm, that corresponds to a stacking of 4 to 5 hybrid layers. Furthermore, the variation of the Bragg peaks toward the low q values as the C8G1 concentration increases, indicating that the interlamellar distance increases from 8 to 12 nm which is comparable to the elongation of the larger semi-axis of C8G1 micelles observed upon increasing C8G1 concentration.[38,39] Nevertheless, it is worth noting that micelle-type arrangements behave as highly dynamic and adaptable systems where size, shape, and aggregation number can be varied through very weak external stimuli such as composition. In our case, the presence of the chaotropic {Mo_{154}} ions with its procession of 14 Na^+ counter-cations should alter the structural parameters of the micelle-type assembly, compared to those determined previously from C8G1-water solutions. Then, the differences observed between the experimental interlamellar distances and those predicted from the proposed geometrical model are small enough (less than 1 nm) to give a fair consistency to these structural hypotheses.

At last, for the concentrations of C8G1 surfactant higher than 50 mM, the Bragg peaks disappear in favor of the typical SAXS pattern of large aggregates characterized by the increase in the scattering intensity in the low q domain (see Figure 3c). At 60 mM, the lamellar ordering is nearly lost to give a small coherence domain as shown by very broad residual peaks. Interestingly, the scattering intensity exhibits a clear q^{-2} dependence of 2D planar structures. This means that the {Mo_{154}} units remain assembled into large isolated 2D structures, probably reminiscent of those involved previously within the lamellar mesophase. To sum up, an increase in the C8G1 concentration produces (i) an increase in the length of the C8G1 rod-like micelles which subsequently leads to a

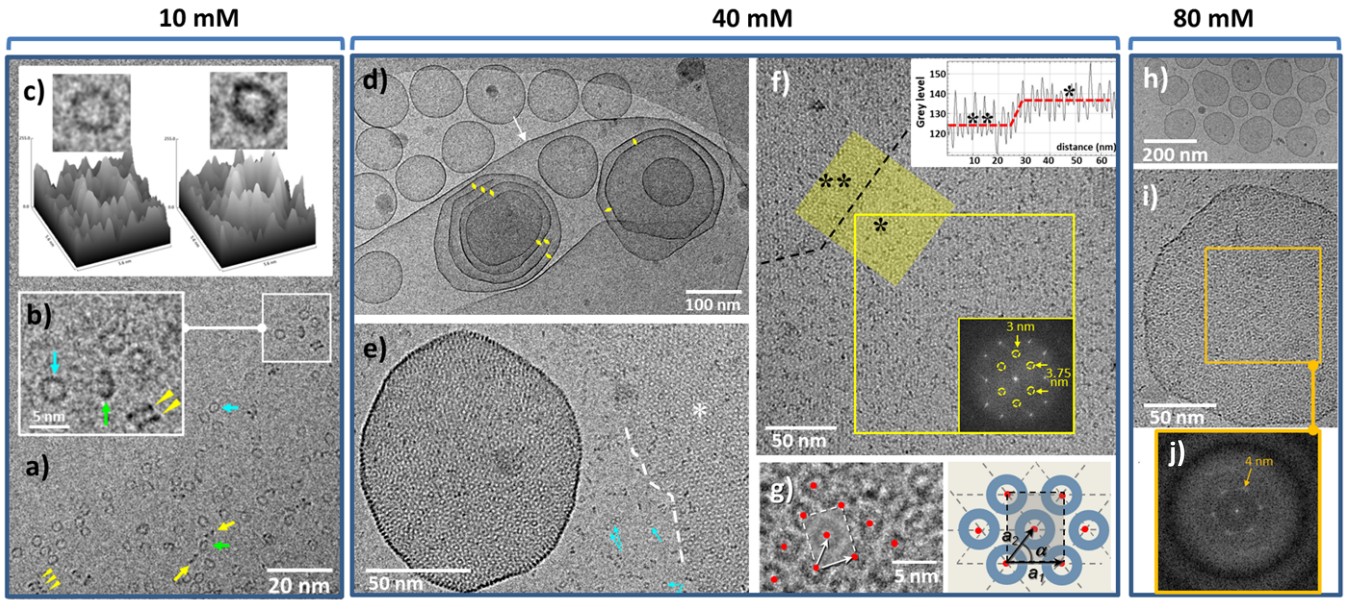

Figure 4. Cryo-electron microscopy of {Mo_{154}}/C8G1 mixture containing 1 mM {Mo_{154}} and 10, 40 or 80 mM C8G1. **10 mM:** (a, b) large field of view and detail showing {Mo_{154}} rings observed in top (cyan arrows), oblique (green) and side (yellow) views. Side views reveal rings isolated (yellow arrows) and stacked on top of each other (yellow arrowheads). (c) Surface plots of top views highlight variations of signal intensity characteristic of isolated (left) and stacked (right). **40 mM:** (d) general view showing coexistence of close nano-objects such as unilamellar, multilamellar vesicles, large crystalline sheets and isolated rings. Folded sheets are identified by white arrows while onion-like vesicles show inter-lamellar regular spacing of 13 ± 2 nm in length (yellow diamond). (e) High magnification reveals crystalline sheets forming vesicles (left) and monolayers (right, *, boundary underlined by the dotted line) surrounded by isolated {Mo_{154}} entities (cyan arrows). (f) Crystalline sheet (*) with a superimposed sheet (top, **); inserts: line profile along the yellow surface showing a step at the edge of the superimposed second sheet. Fourier transform of the monolayer reveals a periodic lattice whose geometrical parameters are consistent with a centered rectangular 2D plane. (g) Detail of the lattice (a_1 = 4.7 nm, a_2 = 3.8 nm and α = 52°), deriving from the hexagonal plane identified by single-crystal X-ray diffraction analysis (a_1 = a_2 = 4.1 nm and α = 60°). **80 mM:** (h) General view of isolated unilamellar vesicles. Onion-like structures are still present but in smaller quantities. (i), High magnification reveals a curved ordered sheet forming a {Mo_{154}}-based vesicle. (j) Fourier transform of orange square in (i) revealing a hexagonal arrangement with a lattice parameter of 4.6 nm.

increase in the interlamellar smectic distance. Ultimately, the hybrid lamellar smectic ordering is exfoliated into dispersed {Mo_{154}}-based nanosheets stabilized by two layers of rod-like micelles on both sides (see Figure 3c). Besides, SAXS investigations performed on 0.5 mM {Mo_{154}} solution never revealed the formation of this striking lamellar phase. In these conditions, the {Mo_{154}}/C8G1 mixtures show only {Mo_{154}}-based aggregates that convert directly into exfoliated C8G1-{Mo_{154}} layers (not shown). These observations and related scenarios are fairly consistent with the cryo-TEM observations while ^{1}H NMR experiments, viscosity measurements, and tensiometry analysis reflect in somehow the different behavior of a 1 mM aqueous solutions in {Mo_{154}} along the C8G1 content (see below).

Cryo-TEM observation. The cryo-electronic microscopy completes nicely the SAXS data, showing the structural richness of the C8G1-{Mo_{154}} system. The cryo-TEM investigation was carried out to explore the three compositional domains evidenced previously by SAXS and corresponding to 1 mM in {Mo_{154}} mixed with 10, 40, and 80 mM in C8G1, respectively. Full details about the preparation and acquisition of cryo-TEM images are given in SI, section I.2.6. For 10 mM in C8G1, the landscape of cryo-electron microscopy images reveals predominantly isolated {Mo_{154}} wheels, well identified as dark toroids around 3.5 nm in diameter (see Figure 4a). In addition, these wheel-shaped clusters exhibit no preferential orientations, being top, oblique, or side oriented (see Figures 4b-c). However, slightly staggered stacks of two or three wheels can be observed very rarely. These {Mo_{154}} cryo-TEM observations are in fair agreement with those carried out by scanning tunneling microscopy (STM) previously reported by Müller *et al.*[40] Increasing the C8G1 concentration up to 40 mM, the scenario becomes significantly different as the C8G1-{Mo_{154}} system exhibits the coexistence of different types of material such as close vesicles, large crystalline sheets and some persistent isolated {Mo_{154}} rings (see Figure 4d). Vesicle size distribution ranges from 40 to 900 nm consistent with high polydispersity. In addition, some hollow unilamellar vesicles can be observed, while striking onion-shaped arrangements are also frequently found. These latter soft matter systems can be also described as multilamellar vesicles showing almost regular inter-lamella spacing reaching around 13 ± 2 nm in length (see Figure 4d) which is in full agreement with the interlamellar spacing determined by SAXS (see Figure 3b). Besides, cryo-TEM imaging reveals also large crystalline sheets that extend over micron-scale distances (see Figures 4e-f). High imaging magnification shows that these sheets can stack to on top of each other as shown by the line profile which evidences clearly a step resulting from two superimposed planes (see Figure 4f) or fold up into open vesicles that could correspond to a snapshot of vesicle formation from a flexible sheet (see SI, Figure S7). Furthermore, single sheets,

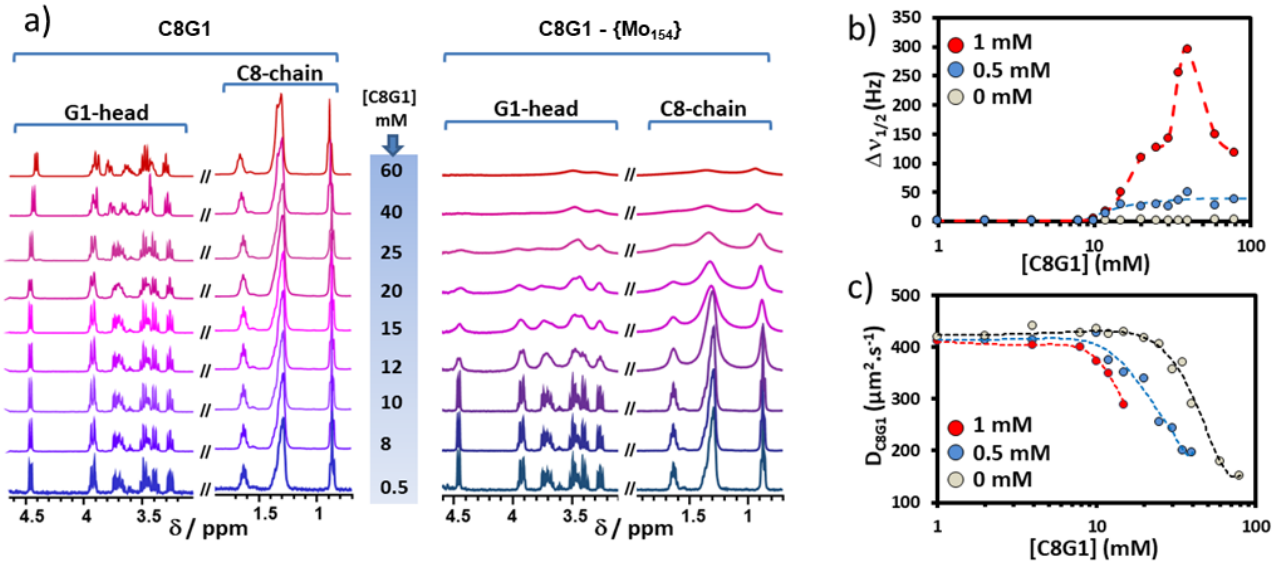

Figure 5. ^{1}H NMR evidence of formation of POM-based hybrid aggregates including C8G1 species as surfactant. a) ^{1}H NMR spectra of C8G1 (298 K, 400 MHz, D_2O) recorded in the 0.5-60 mM concentration range in C8G1 in absence and presence of 0.5 mM $\{Mo_{154}\}$. While the increase of the C8G1 concentration leads to only tiny changes on the ^{1}H NMR spectra after 20 mM (*cmc*), the presence of 0.5 mM $\{Mo_{154}\}$ ring-shaped anion provokes an abrupt broadening of the overall resonances starting at 10 mM, highlighted in b) showing the variation of the C8G1 averaged line broadening observed for 0, 0.5 and 1 mM $\{Mo_{154}\}$ aqueous solutions, respectively. c) Self-diffusion coefficients of C8G1 (noted D_{C8G1}) measured by ^{1}H DOSY NMR revealing the successive decrease of the critical concentration from 23 *mM* (*cmc*) to about 8 mM (*cac*) as the $\{Mo_{154}\}$ concentration increase from 0 to 1 mM.

stacked sheets and closed vesicles were unambiguously identified by using analysis of curvature direction or Fourier transform (FT) function of the images (see SI, Figures S8 and S9). Due to their crystalline nature, these vesicles are often facetted with irregular and often not fully closed shapes, reminiscent with those found in other crystalline shells.[41,42] As expected, the Fourier transform (FT) of the monolayer supports the direct observation and indicates a centered rectangular 2D lattice built from $\{Mo_{154}\}$ wheels whose periodic arrangement gives rise to two periodic distances of $a_1 = 4.7$ nm and $a_2 = 3.8$ nm with angle $\alpha = 52°$ (see Figures 4f and 4g). It should be worth noting that this centered rectangular 2D lattice can be viewed as a distortion of the hexagonal planes evidenced by the single-crystal X-ray diffraction analysis of $Na_{14}\{Mo_{154}O_{462}H_{14}(H_2O)_{70}\}\cdot 15C8G1.70H_2O$ ($a_1 = a_2 = 4.1$ nm; $\alpha = 60°$, see Figures 2c and 4g). Although cryo-TEM imaging evidences unambiguously the presence of multilamellar assemblies that are certainly at the origin of the Bragg peaks observed on scattering data,[43,44] we note that such systems are not predominant. There are several possible reasons for this. Cryo-TEM observations are carried out on the thinnest region of the specimen, from which gelled multilamellar aggregates may be excluded. Furthermore, unfavorable preferential top views of the multistacked assemblies prevent direct measurements of the lamellar stacking distance. Finally, observation of the 40 mM C8G1 sample reveals that all these coexisting nanosized objects, i.e., uni- and multilamellar vesicles, folded and unfolded sheets appear very close to each other as if they are components of a unique system (see Figure 4d). The mean distance of separation lies within 8-13 nm which corresponds to the dimension of the C8G1-based type micelles. According to the previous structural hypothesis formulated from SAXS data to explain the diffraction peaks, these different objects (sheets, vesicles) could stack at regular spacing, interconnected by C8G1-based micelles. Furthermore, such a hypothesis could also explain nicely the gelling state which occurs only in this concentration range. Then, for a higher concentration in C8G1, the solution becomes fluid again. Thus, the cryo-TEM images resulting from 80 mM C8G1 solution shown in Figure 4h are characterized by numerous unilamellar vesicles that appear smaller with an average diameter of around 120 nm compared to those of around 160 nm observed for the 40 mM sample. Multilamellar vesicles are still present but much less numerous than unilamellar vesicles. These vesicles are also built from a single sheet of $\{Mo_{154}\}$-C8G1 that described the local hexagonal curved plane, characterized by an inter-ring distance of 4.6 nm (see Figures 4i-j). Furthermore, in such conditions, the average distance of separation between these nano-objects appears significantly larger, by spreading between 10 and 40 nm. This observation could be related to the exfoliation process of the stacked planes which has been proposed to explain the sudden disappearance of the diffraction peaks from the SAXS profiles (see Figure 3c). This exfoliation process can also be invoked to convert the multilamellar into unilamellar vesicles and to explain the increase in the inter-vesicle distances. This nano-structuring, leading mainly to isolated nano-objects, is also consistent with the decrease in viscosity where a gel-fluid transition was observed for C8G1 concentrations above 60 mM (see below and Figure 7).

NMR investigations. ^{1}H NMR study has been undertaken to give complementary insights about the local environment of the surfactant within the $\{Mo_{154}\}$-containing bulk solution. Full information and details concerning NMR (DOSY and 1D spectra) are supplied in SI, sections 1.2.1 and 1.3.2. The DOSY NMR analyses carried out from the C8G1 ^{1}H NMR resonances (see Fig. 5c) reveal a classical behavior for non-ionic surfactant that

consists of nearly constant self-diffusion coefficient values of C8G1 (noted D_{C8G1}) until the *cmc* value, clearly discernible at about 25 mM by an abrupt decrease of D_{C8G1} from about 415 to 150 $\mu m^2.s^{-1}$ in 80 mM C8G1 aqueous solution. Above the *cmc*, the continuous decrease of D_{C8G1} might be due to micellar growing that reduces the translational mobility of surfactant embedded within micellar aggregates.[45] In the presence of 0.5 mM $\{Mo_{154}\}$ nano-ring, variation of the self-diffusion coefficient D_{C8G1} adopts a similar pattern featured by a breaking point at 12 mM, significantly lower than that observed for the C8G1 *cmc*. Increasing the $\{Mo_{154}\}$ concentration up to 1 mM leads to a similar behavior showing a decrease of D_{C8G1} occurring as soon as about 8 mM. These breaking points must be understood as a *critical aggregation concentration* (*cac*) corresponding to the sudden formation of the hybrid C8G1-$\{Mo_{154}\}$ aggregates. It is worth noting that in such conditions (1 mM in $\{Mo_{154}\}$), using concentrations higher than 20 mM in C8G1 provokes huge broadening of the ^{1}H NMR resonances that prevents any reliable DOSY analysis in this concentration region. In addition, analysis of NMR line widths (noted $\Delta\nu_{1/2}$) appears also instructive about evidencing any intermolecular interactions and subsequent changes in the colligative properties. In $\{Mo_{154}\}$ free solutions, C8G1 ^{1}H NMR spectra reveal only minor changes below and above the *cmc* (see Figure 5A). In contrast, the presence of $\{Mo_{154}\}$ causes a marked alteration of all the C8G1 resonances, including those of the glucosidic head (G1 part) and the aliphatic chain (C8 part), which undergo an abrupt broadening at a *cac* observed at about 10 mM. These variations shown in Figure 5b, such as the $\Delta\nu_{1/2}$ values averaged over the G1 or C8 moieties resonances should reflect the alteration of the correlation time τ_c of the C8G1 species, which is a direct measurement of the intimate molecular motions such as free rotation (for nearly spherical objects) or internal molecular fluctuations arising along the σ-bonds. As shown in Figure 5a, interactions in $\{Mo_{154}\}$-free solution, occurring between C8G1 flexible species in micellar aggregates do not alter significantly the correlation time since $\Delta\nu_{1/2}$ linewidths appear quite unaffected above the *cmc* value (see Figures 5a and 5b). This is a general feature of micelle-based materials which exhibit a liquid-like behavior. On the contrary, the large broadening of the C8G1 resonances observed in the presence of C8G1 corresponds to the largest ^{1}H NMR linewidths (see Figure 5b) and to the maximum of viscosity observed for the same composition range (see Figure 7). Above 10 mM in C8G1, data NMR (linewidth and self-diffusion coefficient) should be consistent with the quasi-immobilization of the C8G1 surfactant within hybrid $\{Mo_{154}\}$-based aggregates. Interestingly, for 1 mM $\{Mo_{154}\}$-containing solutions, we observed the gelling of the solution in the 30-40 mM narrow range for C8G1 concentration while for higher concentrations, the $\{Mo_{154}\}$-C8G1 solutions became fluid again (corresponding ^{1}H NMR spectra are shown in SI, section 2.4, Figure S4). Not fortuitously, the observed gelling domain coincides with the narrow concentration range of about 35-45 mM in C8G1 corresponding to the largest ^{1}H NMR linewidths (see Figures 5b and S4 in SI) and to the maximum of the viscosity observed for the same composition (see below and Figure 7).

ITC study. ITC experiments were carried out at room temperature to highlight the thermochemical fingerprints of the supramolecular events corresponding to disassembly/reassembly processes in the $\{Mo_{154}\}$/C8G1 system. The applied methodology allowed measuring the exchanged heat that occurs from dilution experiments performed from 200 mM C8G1 samples in pure water or in 1 mM aqueous solution of $\{Mo_{154}\}$. The concentrations of the resulting solutions spread over the 0-80 mM range which borders the supramolecular events previously highlighted by SAXS and ^{1}H NMR. Further details about ITC methodologies are given in supporting information, section 1.2.4. In the absence of the $\{Mo_{154}\}$ species, the thermogram exhibits the typical exothermic signature expected for the C8G1 demicellization process which takes place for concentrations lower than 21 mM in C8G1 (see Figure 6).[28] However, when the dilution experiments are performed in 1 mM $\{Mo_{154}\}$ aqueous solution, the ITC signal is strongly altered (see Figure 6) revealing additional thermochemical events which delimit four different domains. For concentrations of C8G1 below 14 mM (domain 1), the ITC pattern is strictly identical to that performed in water consistent with the disassembly of the C8G1 micelles which exhibits exactly the same thermochemical characteristic. This observation suggests there is almost no detectable association between C8G1 and $\{Mo_{154}\}$ in this domain. At around 14 mM, an exothermic jump is observed consistent with the formation of $\{Mo_{154}\}$-C8G1 hybrid aggregates. It must be notated this event appears at C8G1 concentration close to the *cac* determined by NMR. From 14 mM to 25 mM, the overall thermochemical process can be dissected in two successive steps corresponding to i) the disassembly of the C8G1-based micelles into solvated C8G1 surfactants and ii) the formation of hybrid aggregates from supramolecular interactions between solvated C8G1 and $\{Mo_{154}\}$ species. The negative exchanged heat assigned to the later process appears significantly reduced in magnitude compared to that attributed to the C8G1 demicellization. However, this negative value, related to an enthalpy-promoted process well supports the chaotropic effect as the main driving force involved within $\{Mo_{154}\}$-C8G1 supramolecular interactions.[11] Therefore, at about 25 mM, the decrease of the exchanged heat indicates a partial demicellization process, consistent with the coexistence of the hybrid aggregates with C8G1-based micelles. However, the curve breaks at 33 mM showing a weak but significant exothermic thermochemical exchange. This suggests that new types of aggregates based on

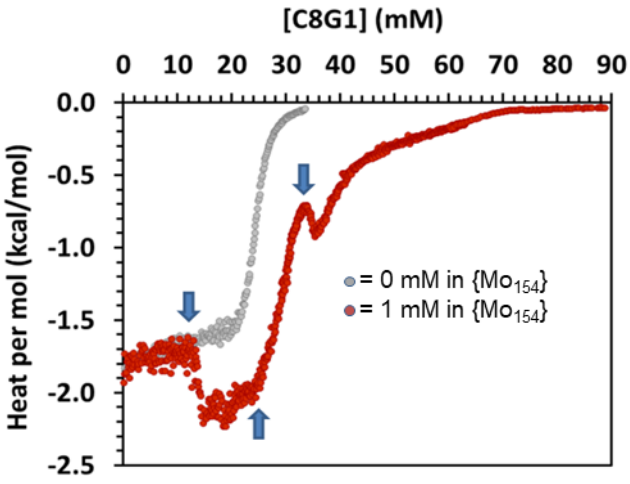

Figure 6. ITC thermograms corresponding to the dilution of a micellar C8G1 solution (200 mM) into pure water (grey curve) or into an aqueous solution of 1 mM $\{Mo_{154}\}$ (red curve). $\{Mo_{154}\}$-containing aqueous solutions reveals three successive events at 14, 27, and 34 mM (blue arrows) while analysis of C8G1 aqueous solutions reveals a critical micellar concentration of 21 mM.

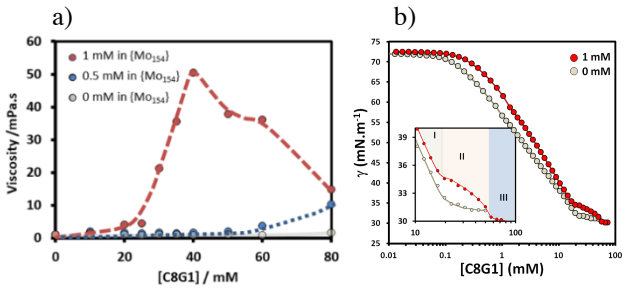

Figure 7. a) Viscosity of Mo_{154} solutions (for 0, 0.5 mM and 1 mM) with different compositions of C8G1 (0–80 mM). Experiments were performed at 25 °C, and the viscosity of the solutions was measured after incubation for 15 min; b) Surface tension variation at the interface of C8G1 aqueous solution at 298 *K* showing the influence of 1 mM $\{Mo_{154}\}$ ring shaped anion upon the classical behavior of the C8G1 surfactant. The shape of $\{Mo_{154}\}$-free C8G1 solution giving a *cmc* value at 23 mM (blue trace) while the presence of $\{Mo_{154}\}$ 1 mM is highlighted by three domains noted I, II and III (red trace and insert) delimited by two kinks at 18 mM and 57 mM, respectively.

$\{Mo_{154}\}$-C8G1 are being formed which could correspond to the formation of the lamellar phase previously identified by SAXS in this composition range. Moreover, the exothermic exchange is also consistent with a desolvation process that takes place occurring as micelle-based aggregates interact with chaotropic $\{Mo_{154}\}$ ions. At last, above 33 mM until 80 mM, the asymptotic return to zero heat is long enough to consider that $\{Mo_{154}\}$-C8G1 assemblies are still evolving in this concentration range which could be linked to the exfoliation process, suggested by the SAXS and cryo-TEM investigations.

Bulk viscosity. The viscosity (noted η) of 1 mM $\{Mo_{154}\}$ aqueous solutions has been measured at room temperature showing the drastic influence of the C8G1 upon the colligative properties of the chemical system (see Figure 7a and SI section 1.3.2 for further details). In $\{Mo_{154}\}$-free solution, the viscosity remains close to that of pure water (approximately 1 cP at $T = 298$ K) in the C8G1 concentration range 0-80 mM of C8G1. In the presence of 0.5 mM in giant blue wheel $\{Mo_{154}\}$, the viscosity tends to increase very slowly with increasing C8G1 concentration, but rises significantly above 50 mM. In contrast, using 1 mM $\{Mo_{154}\}$ aqueous solution, the viscosity drastically increases for C8G1 concentrations above 25 mM and reaches a maximum at around 40 mM in C8G1. Then, variation of the viscosity as a function of the C8G1 concentration can be dissected into three domains that should be related to specific behaviors of the C8G1-$\{Mo_{154}\}$ solutions. The first domain below 20 mM in C8G1 is featured by a negligible change of the viscosity where $\{Mo_{154}\}$ and C8G1 interact to give discrete aggregates. In the second 20-40 mM domain, the viscosity increases abruptly from 4 to 55 mPa.s until reaching a maximum where the C8G1-$\{Mo_{154}\}$ mixtures form fluid gel. This high viscosity state coincides nicely with the maximum of ^{1}H NMR line broadening (see Figure 5b), and also with the domain of the lamellar systems identified by SAXS (see Figure 3b). This increase of internal frictional force must be due to interactions between hybrid $\{Mo_{154}\}$-C8G1 systems, as suggested by cryo-TEM showing multilamellar rigid vesicles or layers that appear closely interconnected (Figure 4d). As expected, further addition of C8G1 induces a decrease of the viscosity from 55 to 17 cP at 80 mM in C8G1 which correlates with the decrease with the ^{1}H NMR line broadening. Such a viscosity decrease indicates that upon the addition of C8G1, the system tends to self-reorganize by reducing the extent of the supramolecular $\{Mo_{154}\}$-C8G1 aggregates with the consecutive increase of the degree of freedom.

Surface tension. The variation of the surface tension of aqueous solution containing 1 mM of $\{Mo_{154}\}$ upon increasing concentration of C8G1 surfactant was measured using the Du Noüy ring technique (see Figure 7b). The results are compared to the evolution of the surface tension of similar C8G1-containing aqueous solution in the absence of $\{Mo_{154}\}$ ion. Upon increasing the concentration of C8G1, the surface tension decreases from that of water ($\gamma \approx 72$ mN·m^{-1}) down to 32 mN·m^{-1} for 23 mM. At higher concentrations, the surface tension remains rather constant. Such an evolution of the surface tension as a function of surfactant concentration is well known, while the kink at 23 mM C8G1 represents the characteristic *cmc* value found in good agreement with the literature.[26,28] As observed by SAXS, ITC, NMR and viscosimetry, in presence of the super-chaotropic $\{Mo_{154}\}$ anion, three distinct regimes are found for C8G1 concentrations in the 0-80 mM range. The first one consists of a quasi-linear continuous decrease of the surface tension until a kink at 18 mM in C8G1, however surface tension variation exhibits a distinct difference with and without $\{Mo_{154}\}$. The presence of $\{Mo_{154}\}$ anion increases significantly the surface tension that could result from bulk-solution interactions between $\{Mo_{154}\}$ and the surfactant inducing a partial C8G1 depletion at the water/air interface. Based on this hypothesis, the change in the surface tension of C8G1 solutions induced by the presence of $\{Mo_{154}\}$ was quantified and suggests that only a few C8G1, about three per $\{Mo_{154}\}$ at most, were able to interact with the giant inorganic ring (see SI, section. 1.3.1). Increasing further the surfactant concentration provokes a drastic change evidenced by the first breaking point. In this second regime, the surface tension seems first to be nearly saturated, then to decrease again until it reaches a second break-point observed at 57 mM in C8G1. This second regime should correspond to the formation of hybrid $\{Mo_{154}\}$-C8G1 nano aggregates identified as a lamellar phase by SAXS and cryo-TEM. At last, for C8G1 concentration above 57 mM, the surface tension reaches a limit value ($\gamma \approx 30$ mN·m^{-1}) that may indicate the formation of C8G1-based micellar systems as usually observed above the *cmc*. Actually, it is worth mentioning that these three domains coincide fairly with the different regimes identified previously by SAXS, ITC, ^{1}H NMR, and viscosity experiments.

CONCLUSION

We have reported that the large wheel-shaped $\{Mo_{154}\}$ exhibits a high affinity for a non-ionic surfactant, i.e., the n-octyl-β–glucoside monomer. Using a convergent set of complementary methods allowed multiscale characterizations that evidence discrete species, well-formed vesicles, large lamellar aggregates, or nanosheets. At low C8G1 concentrations, below 18 mM, surface tension results suggest that up to about three C8G1 interact with one $\{Mo_{154}\}$ anion. Fast dissociative exchange seems to occur, as no change in the ^{1}H NMR signal was observed. Moreover, the C8G1-$\{Mo_{154}\}$ interactions in the low concentration range (below 14 mM) reveal no thermal event by ITC. Formation of another type of hybrid C8G1-$\{Mo_{154}\}$ aggregate occurs abruptly at about 10-15 mM, as shown by ^{1}H NMR and ITC experiments, and at about 18 mM in surface tension. Then, this *critical aggregation concentration* should be understood as the critical micellar concentration resulting from cooperative

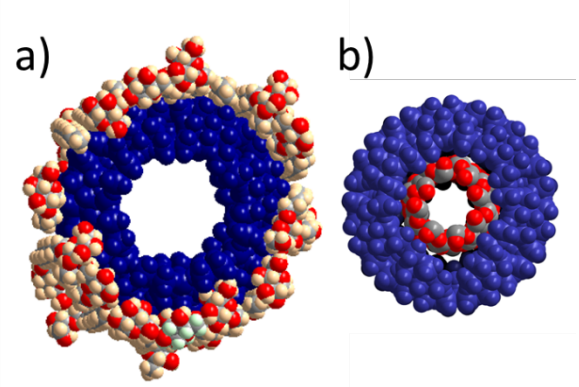

Figure 8. Two structural representations highlighting two options for the rigid ring-shaped {Mo_{154}} anion and non-ionic organic matter; (a) where the inorganic component acts as endoskeleton moiety with outer C8G1 surfactant or as exoskeleton with adapted organic species such as γ-cyclodextrin, closely embedded within the central cavity (see ref. 20).

processes driven by solvent effects. As shown by SAXS, the aggregation process occurring at the *cac* starts with the formation of discrete hybrid species involving single {Mo_{154}} units. However, this situation changes dramatically for greater C8G1 concentration (30-60 mM), by showing the formation of various nano-objects such as unilamellar and multilamellar vesicles, as well as folded and unfolded crystalline sheets (sometimes stacked sheets), as clearly identified by SAXS and cryo-TEM imaging. All these nano-structures result from a lamellar arrangement in which the {Mo_{154}} rings are mutually glued by C8G1 surfactants and pave the nodes of the hexagonal lattice. Such an arrangement has been evidenced by single-crystal X-ray diffraction analysis and identified in the liquid state by high-magnification cryo-TEM images.

Besides, these various nano-objects appear interconnected which results in a gel formation as evidenced by an increase of the viscosity, a decreasing of self-diffusion coefficient of C8G1, and a broadening of NMR signals. Therefore, in the presence of the super-chaotropic ion {Mo_{154}}, the aggregation pathway of C8G1 surfactant proceeds along a complex scenario mainly directed by the primary interactions between the POM species and the non-ionic surfactants. Interestingly, the comprehensive study of the C8G1-{Mo_{154}} behavior over the composition scale has been supported by a single-crystal X-ray diffraction analysis which brings relevant and decisive information about the successive structural snapshots showing i) the discrete aggregates resulting from exposed surfactant molecules glued on the outer surface of the POM, ii) the formation of the {Mo_{154}}-C8G1 layers and vesicles and iii) the lamellar arrangement of the hybrid layers into onion-like structure or 3D packing. In addition, the phase transitions based on the primary interactions between POMs and C8G1 surfactants, leading either to the discrete arrangements in the 10-20 mM range or to the extended nano-arrangements in the 30-40 mM, correspond both to exothermal processes $\Delta_r H < 0$. It is worth noting that such a thermochemical event is fairly consistent with this so-called chaotropic effect that arises from a solvent effect.[46] Due to the super-chaotropic nature of this {Mo_{154}} ion,[21] the solvent effect is strong enough to amplify the conglomerate of weak attractive interactions between the POM and the surfactant.

For higher C8G1 concentration (> 60 mM), a gel-to-fluid phase transition occurs as a result of an increase in the interlamellar space and subsequent exfoliation of the multilamellar assembly.

According to the complementary investigations, these two successive fluid-to-gel and gel-to-fluid phase transitions are believed to be dominated by the interactions between the hybrid nano-objects and C8G1-type micelles. Convincingly, this super-chaotrope {Mo_{154}} macroion interacts strikingly with non-ionic organic substrates, either through outer interface with monomeric species or through its inner surface with adapted substrate like cyclodextrins[21,23] (see Figure 8). It has also been demonstrated that the cooperative self-assembly process driven by the super-chaotropic nature of the {Mo_{154}} ion is capable of producing large vesicles or planes whose membrane is built from well-ordered {Mo_{154}} ions embedded in a "head-to-tail" surfactant monolayer. In addition, this type of monolayer offers interesting perspectives for the design of selective membranes built from active {Mo_{154}} pores that offer both plugged or unplugged options.[21]

At last, such a study provides new fundamental insights into the interactions of polyoxometalates with the biological world that should be reconsidered under the prism of the chaotropic nature of this class of nanoions.

ASSOCIATED CONTENT

Supporting Information.

Materials and methods (tensiometry, viscosimetry, NMR, crystallography, SAXS, Cryo-TEM, elemental analysis, FT-IR spectra, TGA) and author contributions.

"This material is available free of charge via the Internet at http://pubs.acs.org." For instructions on what should be included in the Supporting Information as well as how to prepare this material for publication, refer to the journal's Instructions for Authors.

AUTHOR INFORMATION

Corresponding Author:

emmanuel.cadot@uvsq.fr

Author Contributions

The manuscript was written through contributions of all authors. / All authors have approved the final version of the manuscript and their respective contributions are given in SI (see section 3).

ACKNOWLEDGMENT

We acknowledge SOLEIL Synchrotron for providing access to beamtime and synchrotron radiation facilities on the PROXIMA-2 beamline for the single-crystal X-ray diffraction experiments and analysis. The authors gratefully acknowledge LabEx CHARMMMAT (Grant No. ANR-11-LBX-0039), CNRS-MOMENTUM program, ANR-PRCI CHAOPOM (grant ANR-22-CE92-0043). This work was also supported by (i) University of Versailles Saint Quentin, (ii) CNRS, (iii) Region Ile de France through DIM Nano K. At last, the authors fully acknowledge financial support from the CNRS-CEA network for transmission electron microscopy and atom probe studies (METSA, FR CNRS 3507) on the LPS cryo-EM plateform.

ABBREVIATIONS

C8G1, n-octyl-β−glucoside; POM, polyoxometalate; SAXS, small angle X-ray scattering: ITC, isothermal titration calorimetry.

REFERENCES

(1) Frazzon, J.; Dean, D. R. Formation of Iron–Sulfur Clusters in Bacteria: An Emerging Field in Bioinorganic Chemistry. *Curr. Opin. Chem. Biol.* **2003**, *7* (2), 166–173.

(2) Zhong, W.; Alexeev, D.; Harvey, I.; Guo, M.; Hunter, D. J. B.; Zhu, H.; Campopiano, D. J.; Sadler, P. J. Assembly of an Oxo–Zirconium(IV) Cluster in a Protein Cleft. *Angew. Chem. Int. Ed.* **2004**, *43* (44), 5914–5918.

(3) Barba-Bon, A.; Salluce, G.; Lostalé-Seijo, I.; Assaf, K. I.; Hennig, A.; Montenegro, J.; Nau, W. M. Boron Clusters as Broadband Membrane Carriers. *Nature* **2022**, *603* (7902), 637–642.

(4) Hannon, M. J. Metal-based anticancer drugs: From a past anchored in platinum chemistry to a post-genomic future of diverse chemistry and biology. *Pure Appl. Chem.* **2007**, *79* (12), 2243–2261.

(5) Bijelic, A.; Aureliano, M.; Rompel, A. Polyoxometalates as Potential Next-Generation Metallodrugs in the Combat Against Cancer. *Angew. Chem. Int. Ed.* **2019**, *58* (10), 2980–2999.

(6) de Q. Silveira, G.; Ramesar, N. S.; Nguyen, T. D.; Bahng, J. H.; Glotzer, S. C.; Kotov, N. A. Supraparticle Nanoassemblies with Enzymes. *Chem. Mater.* **2019**, *31* (18), 7493–7500.

(7) Lehn, J.-M. Supramolecular Chemistry—Scope and Perspectives Molecules, Supermolecules, and Molecular Devices (Nobel Lecture). *Angew. Chem. Int. Ed. Engl.* **1988**, *27* (1), 89–112.

(8) Polarz, S.; Landsmann, S.; Klaiber, A. Hybrid Surfactant Systems with Inorganic Constituents. *Angew. Chem. Int. Ed.* **2014**, *53* (4), 946–954.

(9) Webber, M. J.; Langer, R. Drug Delivery by Supramolecular Design. *Chem. Soc. Rev.* **2017**, *46* (21), 6600–6620.

(10) Jing, B.; Hutin, M.; Connor, E.; Cronin, L.; Zhu, Y. Polyoxometalate Macroion Induced Phase and Morphology Instability of Lipid Membrane. *Chem. Sci.* **2013**, *4* (10), 3818–3826.

(11) Assaf, K. I.; Ural, M. S.; Pan, F.; Georgiev, T.; Simova, S.; Rissanen, K.; Gabel, D.; Nau, W. M. Water Structure Recovery in Chaotropic Anion Recognition: High-Affinity Binding of Dodecaborate Clusters to γ-Cyclodextrin. *Angew. Chem. Int. Ed.* **2015**, *54* (23), 6852–6856.

(12) Moussawi, M. A.; Leclerc-Laronze, N.; Floquet, S.; Abramov, P. A.; Sokolov, M. N.; Cordier, S.; Ponchel, A.; Monflier, E.; Bricout, H.; Landy, D.; Haouas, M.; Marrot, J.; Cadot, E. Polyoxometalate, Cationic Cluster, and γ-Cyclodextrin: From Primary Interactions to Supramolecular Hybrid Materials. *J. Am. Chem. Soc.* **2017**, *139* (36), 12793–12803.

(13) Hohenschutz, M.; Grillo, I.; Diat, O.; Bauduin, P. How Nano-Ions Act Like Ionic Surfactants. *Angew. Chem. Int. Ed.* **2020**, *59* (21), 8084–8088.

(14) Khlifi, S.; Marrot, J.; Haouas, M.; Shepard, W. E.; Falaise, C.; Cadot, E. Chaotropic Effect as an Assembly Motif to Construct Supramolecular Cyclodextrin-Polyoxometalate-Based Frameworks. *J. Am. Chem. Soc.* **2022**, *144* (10), 4469–4477.

(15) Fang, X.; Kögerler, P.; Isaacs, L.; Uchida, S.; Mizuno, N. Cucurbit[n]uril−Polyoxoanion Hybrids. *J. Am. Chem. Soc.* **2009**, *131* (2), 432–433.

(16) Hohenschutz, M.; Dufrêche, J.-F.; Diat, O.; Bauduin, P. When Ions Defy Electrostatics: The Case of Superchaotropic Nanoion Adsorption. *J. Phys. Chem. Lett.* **2023**, *14* (15), 3602–3608.

(17) Solé-Daura, A.; Poblet, J. M.; Carbó, J. J. Structure–Activity Relationships for the Affinity of Chaotropic Polyoxometalate Anions towards Proteins. *Chem. – Eur. J.* **2020**, *26* (26), 5799–5809.

(18) Yao, S.; Falaise, C.; Ivanov, A. A.; Leclerc, N.; Hohenschutz, M.; Haouas, M.; Landy, D.; Shestopalov, M. A.; Bauduin, P.; Cadot, E. Hofmeister Effect in the Keggin-Type Polyoxotungstate Series. *Inorg. Chem. Front.* **2021**, *8* (1), 12–25.

(19) Müller, A.; Krickemeyer, E.; Meyer, J.; Bögge, H.; Peters, F.; Plass, W.; Diemann, E.; Dillinger, S.; Nonnenbruch, F.; Randerath, M.; Menke, C. $[Mo_{154}(NO)_{14}O_{420}(OH)_{28}(H_2O)_{70}]^{(25\pm5)-}$: A Water-Soluble Big Wheel with More than 700 Atoms and a Relative Molecular Mass of About 24000. *Angew. Chem. Int. Ed. Engl.* **1995**, *34* (19), 2122–2124.

(20) Muller, A.; Das, S. K.; Fedin, V. P.; Krickemeyer, E.; Beugholt, C.; Bogge, H.; Schmidtmann, M.; Hauptfleisch, B. Rapid and Simple Isolation of the Crystalline Molybdenum-Blue Compounds with Discrete and Linked Nanosized Ring-Shaped Anions: $Na_{15}[Mo^{VI}_{126}Mo^{V}_{28}O_{462}H_{14}(H_2O)_{70}]_{0.5}[Mo_{124}Mo_{28}O_{457}H_{14}(H_2O)_{68}]_{0.5}.400H_2O$ and $Na_{22}[Mo_{118}Mo_{28}O_{442}H_{14}(H_2O)_{58}].250H_2O$. *Z. Anorg. Allg. Chem.* **1999**, *625* (7), 1187–1192.

(21) Falaise, C.; Khlifi, S.; Bauduin, P.; Schmid, P.; Shepard, W.; Ivanov, A. A.; Sokolov, M. N.; Shestopalov, M. A.; Abramov, P. A.; Cordier, S.; Marrot, J.; Haouas, M.; Cadot, E. "Host in Host" Supramolecular Core–Shell Type Systems Based on Giant Ring-Shaped Polyoxometalates. *Angew. Chem. Int. Ed.* **2021**, *60* (25), 14146–14153.

(22) Liu, T.; Diemann, E.; Li, H.; Dress, A. W. M.; Müller, A. Self-Assembly in Aqueous Solution of Wheel-Shaped Mo 154 Oxide Clusters into Vesicles. *Nature* **2003**, *426* (6962), 59–62.

(23) Moussawi, M. A.; Haouas, M.; Floquet, S.; Shepard, W. E.; Abramov, P. A.; Sokolov, M. N.; Fedin, V. P.; Cordier, S.; Ponchel, A.; Monflier, E.; Marrot, J.; Cadot, E. Nonconventional Three-Component Hierarchical Host–Guest Assembly Based on Mo-Blue Ring-Shaped Giant Anion, γ-Cyclodextrin, and Dawson-Type Polyoxometalate. *J. Am. Chem. Soc.* **2017**, *139* (41), 14376–14379.

(24) Miras, H. N.; Cooper, G. J. T.; Long, D.-L.; Bögge, H.; Müller, A.; Streb, C.; Cronin, L. Unveiling the Transient Template in the Self-Assembly of a Molecular Oxide Nanowheel. *Science* **2010**, *327* (5961), 72–74. https://doi.org/10.1126/science.1181735.

(25) Miras, H. N.; Mathis, C.; Xuan, W.; Long, D.-L.; Pow, R.; Cronin, L. Spontaneous Formation of Autocatalytic Sets with Self-Replicating Inorganic Metal Oxide Clusters. *Proc. Natl. Acad. Sci.* **2020**, *117* (20), 10699–10705.

(26) Kameyama, K.; Takagi, T. Micellar Properties of Octylglucoside in Aqueous Solutions. *J. Colloid Interface Sci.* **1990**, *137* (1), 1–10.

(27) Garavito R. M. and Ferguson-Miller S. Detergents as tools in membrane biochemistry. *J Biol Chem.* **2001,** 276(35), 32403-32406.
(28) Medeiros, M.; Marcos, X.; Velasco-Medina, A. A.; Perez-Casas, S.; Gracia-Fadrique, J. Micellization and Adsorption Modeling of Single and Mixed Nonionic Surfactants. *Colloids Surf. Physicochem. Eng. Asp.* **2018**, *556*, 81–92.
(29) Rigaud, J.-L.; Pitard, B.; Levy, D. Reconstitution of Membrane Proteins into Liposomes: Application to Energy-Transducing Membrane Proteins. *Biochim. Biophys. Acta BBA - Bioenerg.* **1995**, *1231* (3), 223–246.
(30) Levitzki, A. Reconstitution of Membrane Receptor Systems. *Biochim. Biophys. Acta BBA - Rev. Biomembr.* **1985**, *822* (1), 127–153.
(31) Garavito, R.; Hinz, U.; Neuhaus, J. The Crystallization of Outer-Membrane Proteins from Escherichia-Coli - Studies on Lamb and Ompa Gene-Products. *J. Biol. Chem.* **1984**, *259* (7), 4254–4257.
(32) Naskar, B.; Diat, O.; Nardello-Rataj, V.; Bauduin, P. Nanometer-Size Polyoxometalate Anions Adsorb Strongly on Neutral Soft Surfaces. *J. Phys. Chem. C* **2015**, *119* (36), 20985–20992.
(33) van Koningsveld, H.; Jansen, J. C.; Straathof, A. J. J. Structure of Anhydrous Octyl α-d-Glucopyranoside. A Comparison with Its Hemi- and Monohydrate. *Acta Crystallogr. C* **1988**, *44* (6), 1054–1057.
(34) Jeffrey, G. A.; Yeon, Y. The Crystal Structure of a 1:1 Complex of n-Octylα- and β-d-Glucopyranoside at 123 K. *Carbohydr. Res.* **1992**, *237*, 45–55.
(35) Hoffmann, B.; Milius, W.; Voss, G.; Wunschel, M.; van Smaalen, S.; Diele, S.; Platz, G. Crystal Structures and Thermotropic Properties of Alkyl α-d-Glucopyranosides and Their Hydrates. *Carbohydr. Res.* **1999**, *323* (1), 192–201.
(36) Colliard, I.; Brown, J. C.; Fast, D. B.; Sockwell, A. K.; Hixon, A. E.; Nyman, M. Snapshots of Ce_{70} Toroid Assembly from Solids and Solution. *J. Am. Chem. Soc.* **2021**, *143* (25), 9612–9621.
(37) Yin, P.; Wu, B.; Mamontov, E.; Daemen, L. L.; Cheng, Y.; Li, T.; Seifert, S.; Hong, K.; Bonnesen, P. V.; Keum, J. K.; Ramirez-Cuesta, A. J. X-Ray and Neutron Scattering Study of the Formation of Core–Shell-Type Polyoxometalates. *J. Am. Chem. Soc.* **2016**, *138* (8), 2638–2643.
(38) Giordano, R.; Maisano, G.; Teixeira, J. SANS Studies of Octyl-β-Glucoside and Glycine Micellar Solutions. *J. Appl. Crystallogr.* **1997**, *30* (5 PART 2), 761–764.
(39) D'Aprano, A.; Giordano, R.; Jannelli, M. P.; Magazù, S.; Maisano, G.; Sesta, B. QELS and SANS Studies of Octyl-β-Glucoside Micellar Solutions. *J. Mol. Struct.* **1996**, *383* (1), 177–182.
(40) Zhong, D.; Sousa, F. L.; Müller, A.; Chi, L.; Fuchs, H. A Nanosized Molybdenum Oxide Wheel with a Unique Electronic-Necklace Structure: STM Study with Submolecular Resolution. *Angew. Chem. Int. Ed.* **2011**, *50* (31), 7018–7021.
(41) Hicks, S. D.; Henley, C. L. Irreversible Growth Model for Virus Capsid Assembly. *Phys. Rev. E* **2006**, *74* (3), 031912. https://doi.org/10.1103/PhysRevE.74.031912.
(42) Hagan, M. F.; Zandi, R. Recent Advances in Coarse-Grained Modeling of Virus Assembly. *Curr. Opin. Virol.* **2016**, *18*, 36–43.
(43) Lemmich, J.; Mortensen, K.; Ipsen, J. H.; Honger, T.; Bauer, R.; Mouritsen, O. G. Small-Angle Neutron Scattering from Multilamellar Lipid rBilayers: Theory, Model, and Experiment. *Phys. Rev. E Stat. Phys. Plasmas Fluids Relat. Interdiscip. Top.* **1996**, *53* (5), 5169–5180.
(44) Nele, V.; Holme, M. N.; Kauscher, U.; Thomas, M. R.; Doutch, J. J.; Stevens, M. M. Effect of Formulation Method, Lipid Composition, and PEGylation on Vesicle Lamellarity: A Small-Angle Neutron Scattering Study. *Langmuir* **2019**, *35* (18), 6064–6074.
(45) Bauer, C.; Bauduin, P.; Girard, L.; Diat, O.; Zemb, T. Hydration of Sugar Based Surfactants under Osmotic Stress: A SAXS Study. *Colloids Surf. Physicochem. Eng. Asp.* **2012**, *413*, 92–100.
(46) Assaf, K. I.; Nau, W. M. The Chaotropic Effect as an Assembly Motif in Chemistry. *Angew. Chem. Int. Ed.* **2018**, *57* (43), 13968–13981.

SYNOPSIS TOC (Word Style “SN_Synopsis_TOC”).